Subproject F3.3

Nanocrystalline Composites Containing SnO_2 as New Anode Materials for Li-Ion Batteries

Principle Investigators: Sylvio Indris, Anne S. Ulrich, Horst Hahn

CFN-Financed Scientists: S. Becker (3/4 TVÖD13, 25 months),

Further Scientists: Dr. Marco Scheuermann

Institute of Nanotechnology, Karlsruhe Institute of Technology

Institute of Organic Chemistry, Karlsruhe Institute of Technology

Institute of Biological Interfaces (IBG-2), Karlsruhe Institute of Technology

F3.3 Indris, Ulrich,
Hahn

Nanocrystalline Composites Containing SnO_2 as New Anode Materials for Li-Ion Batteries

Introduction and Summary

The development of mobile electronic devices (notebooks, mobile phones, etc.) is strongly related to the improvement of lithium-ion batteries. The electrode materials that are capable of inserting lithium have to be optimized in order to achieve the required parameters for applications.. The use of nanocrystalline materials allows for a faster lithium insertion/extrusion due to the shorter diffusion pathways, resulting in a higher power density. SnO_2 is a promising candidate for the use as an anode material in Li ion batteries since it has a high theoretical specific charge capacity. According to the subsequent reactions

$$4\,Li + SnO_2 \rightarrow 2\,Li_2O + Sn\,, \qquad 4.4\,Li + Sn \rightarrow Li_{4.4}Sn$$

a total of 8.4 Li ions can be inserted per formula unit SnO_2. This corresponds to a theoretical capacity of 1491 mAh/g. While the second step is fully reversible, the first step will show only partial reversibility. A critical point is the alloy formation that leads to extreme volume changes, a loss of electrical contact and, consequently, a drop in the capacity after several cycles. While SnO_2 has a potential for a high capacity storage material, it also allows the detailed examination of the underlying mechanisms using a variety of characterization methods, including in-situ and ex-situ XRD, Mössbauer spectroscopy using ^{119}Sn-probe atoms and both ^{7}Li- and ^{119}Sn-NMR. Different strategies can be pursued to overcome the problems related to the volume changes during charging and discharging: (i) The use of ultra-fine particles with small absolute volume changes. (ii) The use of composites with SnO_2 embedded in a matrix that can accommodate the volume changes.

We pursued a strategy that combines both approaches. Nanocrystalline composites have been prepared by different synthesis methods, including mechanochemical reactions, gas-phase synthesis, and sputtering techniques. In addition to standard battery testing, the underlying electrochemical reaction pathways during Li insertion/removal have been studied by XRD, NMR, Mössbauer spectroscopy, and TEM.

Close cooperations exist with projects F3.1 (cf. Sect. 1) and F3.2.

1. SnO_2 Nanostructures

We studied the local structural disorder and relaxation in different nanostructures of SnO_2 by using ^{119}Sn MAS NMR measurements in combination with ^{119}Sn Mössbauer spectroscopy. We investigated nanocrystalline powders with an average crystallite size of 8 nm as well as hollow spheres with a wall thickness of 3 nm and a diameter of 14 nm, and compared the results to coarse-grained materials. While the uniform SnO_6 octahedra in the coarse-grained material show a well-known distortion and thus large electric field gradients, the nanocrystalline SnO_2 exhibits a structural relaxation leading to a distribution of local environments and more symmetric octahedra. The SnO_2 hollow spheres show strong local disorder in combination with highly asymmetric environments around the Sn atoms.

SnO_2 nanoparticles were prepared by means of chemical vapour synthesis using tetramethyltin (TMT, $Sn(CH_3)_4$, >99.0%, Sigma-Aldrich) as precursor material. SnO_2 hollow spheres were prepared in a water-in-oil microemulsion utilizing cetyltrimethylammoniumbromide (Aldrich, 95 %) as a surfactant and hexanol (Fluka, >98 %) as a co-surfactant as well as *n*-dodecane (Aldrich, >99 %) as the non-polar oil-phase. In addition, a 5:1 mixture of methanol (Seulberger, 99 %) and demineralized water was added as the polar phase. To this micellar system a solution of $Sn(Ot\text{-}Bu)_4$

(ABCR, 99.99 %) in dodecane was added dropwise at ambient temperature without stirring. Subsequently, the reaction mixture was left to react for 12 h.

Figure 1 shows the XRD patterns of microcrystalline SnO_2, nanocrystalline SnO_2, and SnO_2 hollow spheres. The pattern of the microcrystalline sample reveals narrow peaks and thus good crystallinity. In contrast to that, the nanocrystalline sample shows strong line broadening typical of small crystallite sizes. Using Scherrer's equation, a crystallite size of about 5 nm can be estimated from the line width. The SnO_2 hollow spheres show even broader peaks that can be hardly distinguished any more.

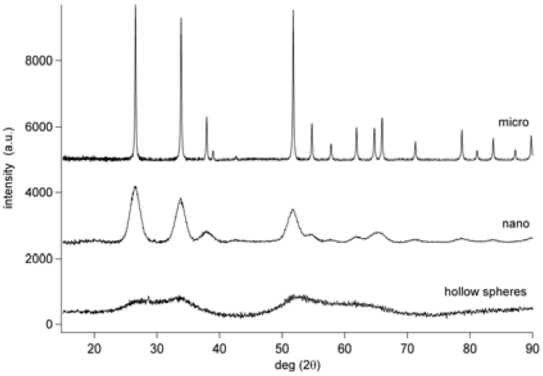

Fig. 1: XRD patterns of microcrystalline SnO_2, nanocrystalline SnO_2, and SnO_2 hollow spheres.

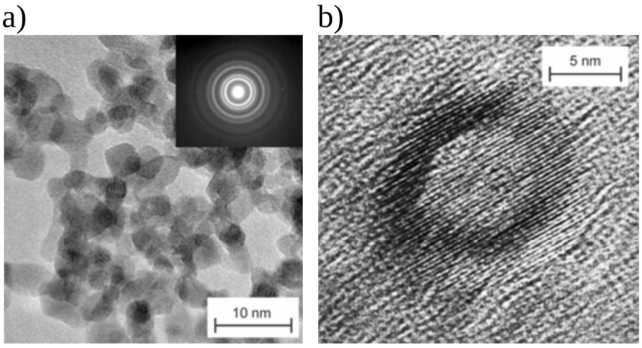

Fig. 2: Transmission electron micrographs of a) nanocrystalline SnO_2 and b) SnO_2 hollow spheres. The insert on the left side shows a typical diffraction pattern.

Figure 2 shows TEM images of nanocrystalline SnO_2 and SnO_2 hollow spheres. For the nanocrystalline SnO_2 (Fig. 3a) the TEM image reveals well-crystallized small particles with an average crystallite size d_0 of 7.7 nm. There is no evidence of amorphous surface layers formed during CVS. The specific surface area of the nanocrystalline SnO_2 is 118 m^2/g. The hollow spheres (Fig. 3b) have an outer diameter of 14 nm and a thickness of about 3 nm, and they also show good crystallinity. Their surface area is 400 m^2/g which indicates that the shells are of porous nature.

The local structure around the Sn atoms was investigated with ^{119}Sn MAS NMR spectroscopy. The results for the three samples are shown in Fig. 3. All samples show a single symmetric peak centered at around -604 ppm being characteristic of the SnO_6 octahedron in the tetragonal structure of SnO_2. For the microcrystalline sample the peak is very narrow with a width of 1.7 ppm. This reveals a high crystallinity with all Sn atoms being located in the same local environment. The nanocrystalline SnO_2 and the SnO_2 hollow spheres show much broader widths of 6.7 ppm and 54 ppm, respectively. This result is indicative that in these samples a large variety of SnO_6 octahedra is present leading to a broad distribution of bond angles and bond lengths. The center of these lines is still at about -604 ppm revealing that the average electron density around the Sn nuclei in the nanostructured samples is identical to the microcrystalline sample.

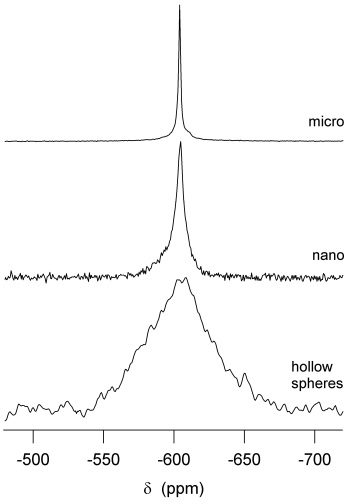

Fig. 3: ^{119}Sn MAS NMR spectra of microcrystalline SnO_2, nanocrystalline SnO_2, and SnO_2 hollow spheres.

Figure 4 shows the results of ^{119}Sn Mössbauer experiments. The ground state of the ^{119}Sn nucleus has a nuclear spin $I = 1/2$ and thus no nuclear quadrupole moment (this is also true for the other NMR active isotopes of Sn, namely ^{115}Sn and ^{117}Sn). Therefore, NMR experiments on this isotope are not sensitive to electric field gradients at the site of the Sn nucleus. In contrast to that, the Mössbauer experiments, making use of the transition from an excited nuclear state with $I = 3/2$ to the ground state, are indeed sensitive to such field gradients.

For each sample the Mössbauer spectrum has to be described with a doublet with overlapping Lorentzian lines. The parameters that result from the corresponding fits (solid lines in Fig. 5) are listed in Tab. 1. For all three samples the isomer shift is close to 0 mm/s, which is characteristic of the SnO_2 structure and in good agreement with the NMR results which show the same average chemical shift for all samples. The microcrystalline sample reveals a quadrupole splitting of 0.53 mm/s which is caused by the asymmetry of the SnO_6 octahedra in the regular structure of well-crystallized SnO_2. This splitting is significantly smaller in the nanocrystalline sample (0.49 mm/s). Thus, the SnO_6 octahedra in the nanocrystalline sample are more symmetric on average, although the local environments around the Sn atoms show a broader distribution, as can be seen from the NMR results. In contrast to that, the SnO_2 hollow spheres show an increased quadrupole splitting of 0.60 mm/s. This reveals strongly distorted SnO_6 octahedra which might indicate a high concentration of point defects.

It is remarkable that the transmission spectra of the samples differ for the three samples. While the total effect in the absorption is about 15% for microcrystalline SnO_2 (Fig. 5), it is much smaller for nanocrystalline SnO_2 (about 1%) and SnO_2 hollow spheres (about 4%). This hints at a strongly reduced Debye-Waller factor in the nanostructured samples and thus to a softening of the crystal lattice. This is in good agreement with the NMR results that show increased structural disorder for the nanostructured samples.

Comparing the NMR results with the Mössbauer results reveals that the structural disorder, reflected by a variation of bond lengths and bond angles, increases when going from the microcrystalline sample to the nanocrystalline sample and is highest for the hollow spheres. In contrast to that, the quadrupole splitting in the Mössbauer spectra, reflecting the average electric field gradient at the site of the Sn nuclei and thus the average asymmetry of the SnO_6 octahedra, shows a different trend. The asymmetry of these octahedra is smaller in the nanocrystalline sample when compared to the microcrystalline sample, but highest in the SnO_2 hollow spheres.

This suggests that a structural relaxation takes place in the near-surface regions of the nanocrystalline SnO_2 particles, leading to variations in the bond lengths and angles, i.e. to local structural disorder, but more symmetric SnO_6 units, on average. The particular morphology of the SnO_2 hollow spheres leads to an even higher degree of local disorder, but the SnO_6 octahedra get highly asymmetric in this case.

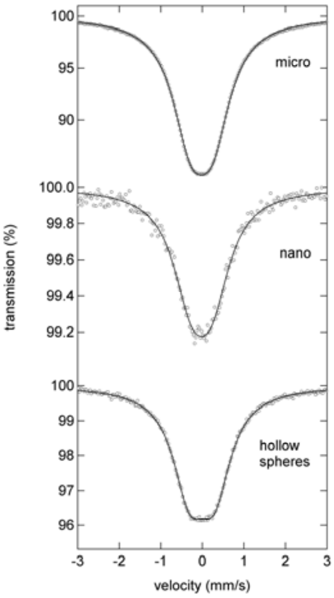

Fig. 4: ^{119}Sn Mössbauer spectra of microcrystalline SnO_2, nanocrystalline SnO_2, and SnO_2 hollow spheres.

Tab. 1: ^{119}Sn Mössbauer parameters of microcrystalline SnO_2, nanocrystalline SnO_2, and SnO_2 hollow spheres. All values are given in mm/s.

	isomer shift	quadrupole splitting	line width
micro	-0.0233 ± 0.0003	0.527 ± 0.001	1.053 ± 0.002
nano	-0.0206 ± 0.0055	0.487 ± 0.023	1.078 ± 0.029
hollow spheres	-0.0117 ± 0.0016	0.600 ± 0.004	0.975 ± 0.007

2. Mechanochemically prepared $ZnO:SnO_2$ composites and Zn_2SnO_4

This sub-project consists of two main parts. In part one the first complete synthesis of Zn_2SnO_4 in a mechanochemical process is presented. Part two reports about the electrochemical characterization of this material used as electrode material in lithium-ion batteries. This characterization includes the techniques of galvanostatic cycling, cyclovoltammetry, XRD, NMR, Mössbauer spectroscopy, and in-situ SEM. Zn_2SnO_4 is an important material in fields like photoelectrochemical cells, photocatalysts and sensor applications. So it is in general desirable to have a simple, fast and cheap way with high yield to synthesize this material. These requirements are fulfilled by the process we used, namely the mechanochemical synthesis. Furthermore, this method operates at relatively low temperature compared to other chemical synthesis routes (Zn_2SnO_4 already has been synthesized by e.g. hydrothermal and solid-state reactions [1,2]).

In our work nanocrystalline Zn_2SnO_4 powders have been prepared by a one-step mechanochemical synthesis. Using the binary precursors SnO_2 and ZnO, together with adequate starting and milling conditions it was possible to synthesize a phase-pure material. The milling was carried out in a planetary ball-mill. For comparison Zn_2SnO_4 was also synthesized in the classical solid-state route. Here a preparation by homogenization and compaction of the reactants is needed as well as a final high – temperature treatment.

The mechanically induced synthesis was followed by XRD (Fig. 5). The pattern of the starting mixture consists of sharp peaks which can be attributed to the bulk SnO_2 and ZnO materials with crystallite sizes of some micrometers. The high energy input of the ball milling system first leads to a decrease in crystallite size of the educt oxides as visible in the peak broadening of the first patterns. In the course of the milling procedure SnO_2 and ZnO particles reach a critical size and a reaction between them is induced. This takes place in the processing time between 1 h and 2 h and leads to the formation of a new complex oxide phase. At the same time the peaks corresponding to the educt materials disappear completely. The pattern of the final product after 4 h is consistent with the JCPDS PDF 24-1470 data of the Zn_2SnO_4 spinel with lattice parameter of 8.657 Å without any additional phase. The crystal structure of the spinel Zn_2SnO_4 belongs to the space group Fd3m. According to the peak broadening the size of crystallites in the Zn_2SnO_4 product was calculated to be about 26 nm (Williamson-Hall method). In Fig. 5 also the comparison with the ceramic Zn_2SnO_4 is given.

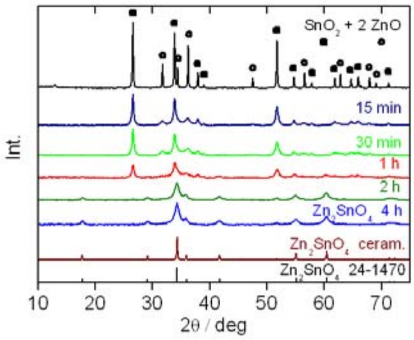

Fig. 5: XRD patterns of SnO_2 + 2 ZnO mixtures milled for various times.

To study the mechanically induced reaction $SnO_2 + 2\,ZnO \rightarrow Zn_2SnO_4$ also ^{119}Sn MAS NMR was applied. This method probes the local structure around the Sn nuclei and reveals changes during the mechanosynthesis. The NMR spectra of samples milled for different times are displayed in Fig. 6.

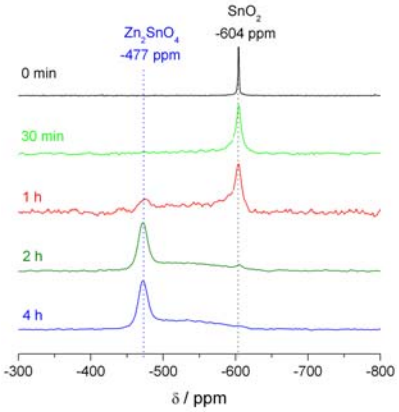

Fig. 6: ^{119}Sn MAS NMR spectra of 2 ZnO + SnO_2 mixtures milled for various times.

The topmost spectrum shows a single peak at -604 ppm, which is consistent with literature data for pure SnO_2. With increasing milling time the peak at -604 ppm decreases and a second peak at -472 ppm together with a broad contribution between -470 ppm and -620 ppm appears. After 4 h of milling the peak at -604 ppm has disappeared completely (bottommost spectrum). As NMR is a very sensitive method to distinguish the different Sn surroundings it is a strong prove that after 4 h the Zn_2SnO_4 synthesis is complete and no educt material is left.

Representative TEM images of the mechanosynthesized product are shown in Fig. 7. They reveal single crystallites with a size in the range of 20 - 40 nm. Furthermore it can be seen that single particles are forming larger agglomerates. The HRTEM image shows the good crystallinity of the particles. The lattice fringes visible in the HRTEM image correspond to the crystallographic (220) plane of Zn_2SnO_4 with d = 3.06 Å (JCPDS PDF 24-1470).

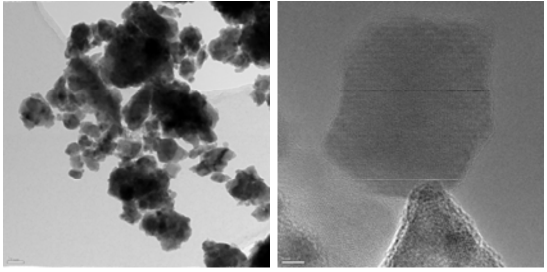

Fig. 7: a) (left) TEM and b) (right) HRTEM image of mechanochemically synthesized Zn_2SnO_4.

Mixtures of SnO_2 and ZnO milled for various times were tested as electrode materials in Li-ion batteries. For comparison, also the Zn_2SnO_4 prepared by a conventional ceramic route was investigated. The samples were continuously discharged and charged against a counter electrode of metallic lithium. In Figure 8 voltage profiles of the first discharging and charging of different samples are shown. The amount of lithium incorporated in the sample material (x) is calculated per formular unit (SnO_2 + 2 ZnO).

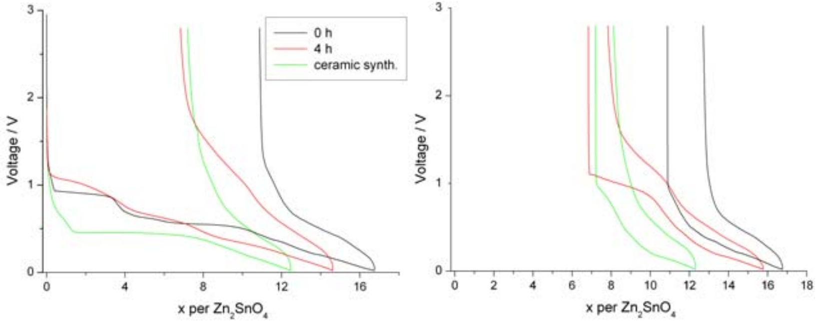

Fig. 8: First and second galvanostatic cycle of SnO_2 + 2 ZnO mixure, mechanosynthesized Zn_2SnO_4 and ceramically synthesized Zn_2SnO_4

The differences in the voltage profiles are clearly visible, concerning shape as well as in the amount of incorporated and released lithium. The unmilled SnO_2/ZnO mixture has a well defined first plateau at about 0.95 V which is known from literature and belongs to the reduction of SnO_2 to metallic Sn and the formation of a Li_2O phase. A second distinct plateau is found at 0.55 V which can be attributed to the reduction of ZnO to Zn. According to literature the following continuous decrease of the voltage corresponds to the alloying process of Li with Sn and Zn [3].

In the case of the mechanosynthesized Zn_2SnO_4 the reduction plateaus are not that distinct anymore. Anyway three main regions are visible, beginning at about 1.1 V, 0.7 V and 0.3 V respectively. The situation looks totaly different in the first cycle of the ceramically synthesized Zn_2SnO_4. One clear plateau appears at 0.45 V followed by a slow decrease in the lower voltage region. The measured irreversible capacity loss in the first cycle of the mechanochemically produced Zn_2SnO_4 is about 581 mAh/g. Thus the coulombic efficiency in the first cycle is 53.4 % which is significantly more than in the case of the educt mixture (34.9 %) and the ceramic route Zn_2SnO_4 (42.4 %). Some reasons for the relatively large irreversible loss of capacity in the first cycle in all materials are probably side reactions with the electrolyte which form the solid electrolyte interphase and the Li_2O phase. The loss of capacity shows the same trend also in the second cycle. It is obvious that the mechanosynthesized Zn_2SnO_4 has got the highest efficiency. Here especially one can recognize a reversible reaction occuring at 1.1 V in contrast to the other samples. This contributes a lot to the overall capacity. The voltage profiles suggest different reactions proceeding in the different samples. To get a more precise picture the various processes were followed also by cyclic voltammetry (CV). In these measurements the sample materials were cycled with a rate of 0.05 mV/s in the voltage range of 0.02 V–2.8 V against Li. Figure 9 shows the first two cycles. In the first cycle the three diffuse reduction plateaus mentioned above for the mechanochemically prepared Zn_2SnO_4 can be easily found.

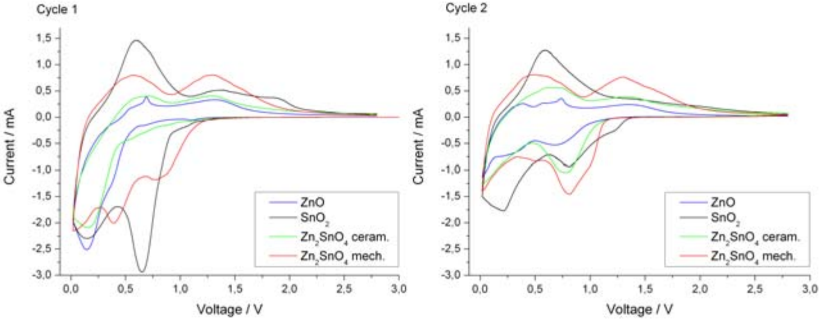

Fig. 9: Cyclic voltammetry of the first (left) and second (right) cycle carried out in the range of 0.02 – 2.8 V (vs Li^+/Li) at a scan rate of 0,05 mV/s) of ZnO and SnO_2 educt material compared to Zn_2SnO_4 prepared mechanochemically and in the ceramic route

In contrast to that, the ceramic Zn_2SnO_4 has one significant reduction peak starting at 0.45 V consistent with the discharging voltage profile. Compared to the mechanochemically prepared sample the first reduction reaction seems to be inhibited.

Considering the SnO_2/ZnO reference the peak visible in the lower voltage region of all samples corresponds probably to alloying processes. In the charging process the de-alloying can be contributed to the first oxidation peak. A remarkable feature of the Zn_2SnO_4 samples is the appearance of a pronounced second oxidation peak beginning at about 1 V. This second reaction is responsible for the smaller capacity loss in the first cycle of the Zn_2SnO_4 compared to the SnO_2/ZnO mixture as already mentioned. In the second cycle the second peak in the reduction of the mechanochemical Zn_2SnO_4 has almost vanished. The behaviour of this material in the second cycle is more similar to the SnO_2 than in the first cycle. Also the reduction peaks in mechanochemically and ceramically prepared Zn_2SnO_4 are more similar than in the first cycle. Again the reversibility of the reaction at 1 V is apparent in the oxidation process in Zn_2SnO_4, especially in the mechanochemical sample. Here the peak has the same intensity as the first oxidation peak. It corresponds to the main reduction peak at about 1 V. The significant oxidation processes indicate that the whole cycling process is more reversible in the mechanochemical Zn_2SnO_4 compared to the other samples. This is also true when having a look at the long-term cycling stability. SnO_2/ZnO mixtures milled for different times and the ceramic Zn_2SnO_4 were cycled against metallic Li in galvanostatic mode. The cycling was carried out in the potential window of 0.02 V–2.8 V vs. Li^+ /Li and the current corresponds to a rate of 6 Li per formular unit Zn_2SnO_4 per 20 h. In Fig. 10 the discharging capacities of the samples are plotted.

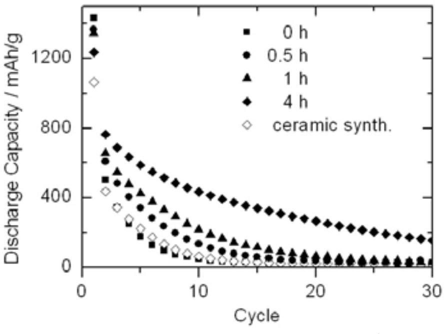

Fig. 10: Discharge capacities of SnO_2+2ZnO mixures milled for various times, as well as of mechano- and ceramically synthesized Zn_2SnO_4

It could be observed that the milling process improved the cycling stability. The discharging and charging capacities increased gradually by prolonged milling of the samples. The mechanosynthesized Zn_2SnO_4 shows considerably better performance compared to the incompletely reacted samples, to pure SnO_2, and also to ceramically synthesized Zn_2SnO_4. One reason for the poor performance of the ceramic sample can be the relatively large crystallite size. It can be derived from the XRD pattern to be in the range of several micrometers. The mechanochemically prepared Zn_2SnO_4 shows the highest specific capacities and the best cycling stability. Nevertheless, also this material shows a continuous decrease in cycling performance. In this context optimizing the morphology of the mechanochemical product by further treatment should be helpful. For example a reduced agglomeration of the nanocrystals should lead to a further improvement of stability. Different methods were applied to compare the electrochemical behaviour of the mechanosynthesized Zn_2SnO_4 during cycling to its structural changes. Concerning the long-range order XRD was applied. Samples with different amount of incorporated lithium were analysed. Figure 11 shows different states during the first discharging and charging. For all the samples the current rates were chosen that way that the first discharge is completed within 100 h.

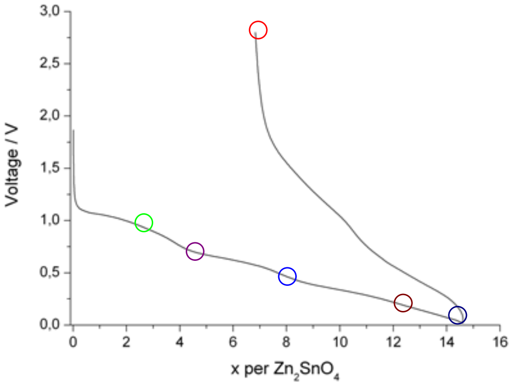

Fig. 11: First constant-current discharge/charge of mechanosynthesized Zn_2SnO_4. Markers indicate states-of-charge characterised by XRD.

The XRD pattern of the mechanosynthesized Zn_2SnO_4 before cycling is consistent with JCPDF 24-1470 (Fig. 12, cf. Fig. 5). During the first reduction step new peaks indicate the formation of metallic Zn (4-0831). The Zn_2SnO_4 spinel structure is still present. The reduction process continues as can be seen for the next pattern. Here the state after the first plateau is displayed. The spinel structure is still dominating but the fraction of the highly crystalline Zn increased. After the second discharging plateau the crystalline Zn phase is by far dominating compared to all other amorphous phases in the pattern. The spinel structure has disappeared almost completely. Just a very small fraction is visible at 18° and 41°2Θ. Thus one can observe an aggregation of Zn metal at this point of discharging.

The situation during the last main discharging reaction is clearly different (x=12.7). While part of Zn still exists, one can also detect peaks corresponding to LiZn alloy (3-0954) as well as $Li_{13}Sn_5$ (29-0838). The broad peaks in the range of about 20°-26° can be attributed to further Li-Sn-alloys. Further amorphous contributions likely come from Li_2CO_3 (01-083-1454) and $LiPF_6$ (01-082-0784). Additional peaks in the pattern represent traces of SnC_2O_4 (22-0496). In the completely discharged sample Zn is not detectable anymore. Peaks in the pattern arise from LiZn, Li-Sn-alloys (most crystalline contributions from $Li_{13}Sn_5$ and Li_5Sn_2, 29-0839), and SnC_2O_4 traces. In the recharged sample it is visible that metallic Zn is the dominant crystalline phase. In addition to that a broad amorphous region (about 20°-35°) remains, probably representing Sn (4-0673), C compounds, Li_2CO_3, and $LiPF_6$.

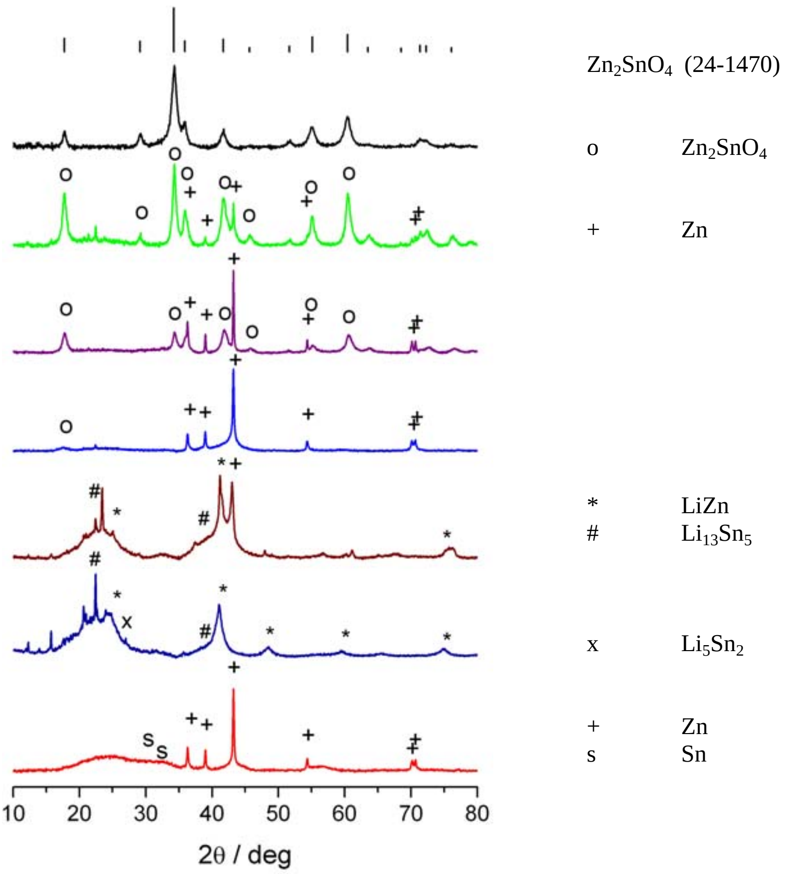

Fig. 12: XRD patterns of mechanosynthesized Zn_2SnO_4 at various states of charge

In summary, the recharged sample is much more amorphous than the initial material. The spinel structure collapses during discharge while Zn and Sn form alloys with Li. After the first charge one can observe an isolation of significant amount of metallic Zn. In the second cycle probably this Zn reacts similarly as in the case of ZnO (compare cyclic voltammetry, figure 5). The isolated reaction of Zn probably leads to the decrease in capacities because of the known low performance of Zn metal. One can suppose that this decreasing effect is even stronger in the case of composite SnO_2/ZnO material in which also metallic Sn is aggregated.

Further methods which were applied to observe structural changes in the materials were ^{7}Li and ^{119}Sn MAS NMR. SnO_2, ZnO and mechanosynthesized Zn_2SnO_4 samples with different amounts of lithium incorporated were investigated. Figure 13 represents states within the first discharge and charge (The particular state is marked in the associated voltage profile). In case of Zn_2SnO_4 all spectra show a peak at 0 ppm, a second peak at approximately 90 ppm is visible in all discharged samples. The recharged sample at the end of the cycle does not show this second peak (bottommost spectrum). For higher lithium contents in the discharged samples a third peak at 40 ppm appears. (Note: Spectral contributions at aproximately +/-450 ppm are MAS sidebands.)

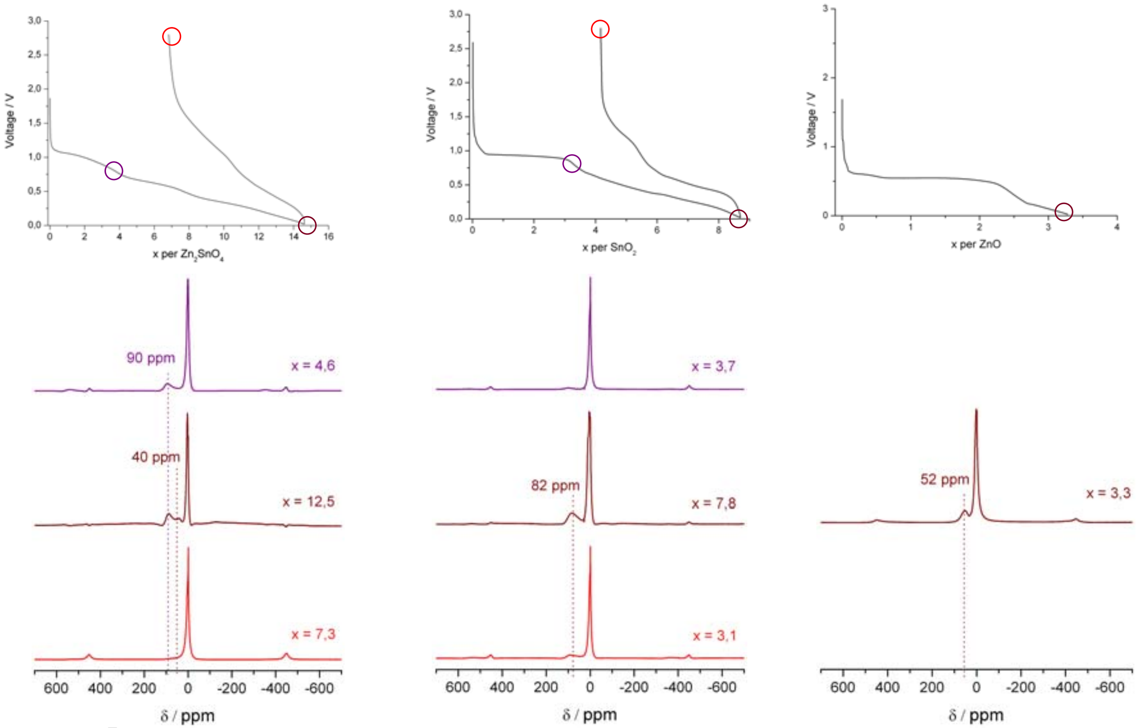

Fig. 13: ^{7}Li MAS NMR of (left) Zn_2SnO_4, (middle) SnO_2, and (right) ZnO samples at different states of charge

The spectrum of the SnO_2 sample with the highest amount of lithium shows two peaks at 4.6 ppm and 82.3 ppm. The analogous discharged ZnO sample shows a similar spectrum with the main peak at 1.5 ppm and a second one at 52 ppm. Therefore in the Zn_2SnO_4 sample one can assign the peak at 90 ppm to Li-Sn compounds similar to the situation in SnO_2. The small peak arrising at 40 ppm represents Li-Zn compounds analogous to ZnO.

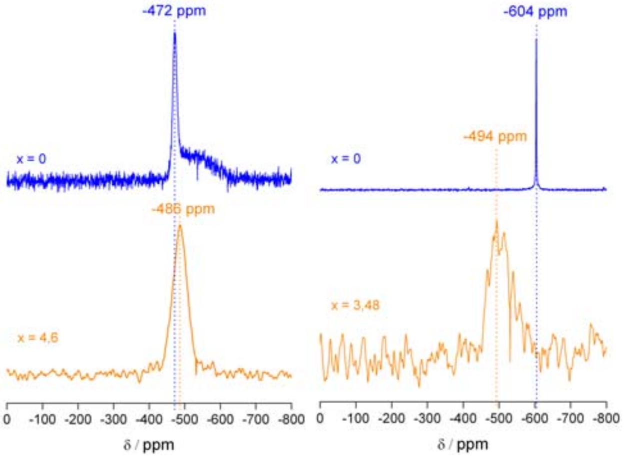

Fig. 14: ^{119}Sn MAS NMR on (left) Zn_2SnO_4 and (right) SnO_2 samples at different states of charge (discharging from top to bottom).

In Figure 14 ^{119}Sn MAS NMR spectra of SnO_2 and mechanosynthesized Zn_2SnO_4 samples intercalated with different amounts of lithium are displayed. Without lithium the Zn_2SnO_4 spectrum shows a peak at -472 ppm and a broad contribution between -470 ppm and -620 ppm (compare Fig. 2). After lithium intercalation the peak slightly shifts, broadens significantly, and the broadband contribution vanishes. In the case of SnO_2 the spectrum of the raw material shows a single peak at -604 ppm. In the given state of discharge it is shifted to -494 ppm, i.e. to a similar position as in

Zn_2SnO_4. The peak also shows an extensive broadening which is even considerably larger than for the Zn_2SnO_4. Thus at the shown states of charge both Zn_2SnO_4 and the SnO_2 contain similar local environments around the Sn nuclei, i.e. the same Li-Sn alloys. The distribution of local environments in Zn_2SnO_4 is not as broad as in SnO_2.

Additionally, the behaviour of mechanosynthesized Zn_2SnO_4 during cycling was followed by *in situ* SEM. The sample was discharged and charged galvanostatically and particles were observed at certain states of charge. Figure 15 shows three different particles. For each one a comparison of two different states is given. All pictures belong to states within the first discharging of the material.

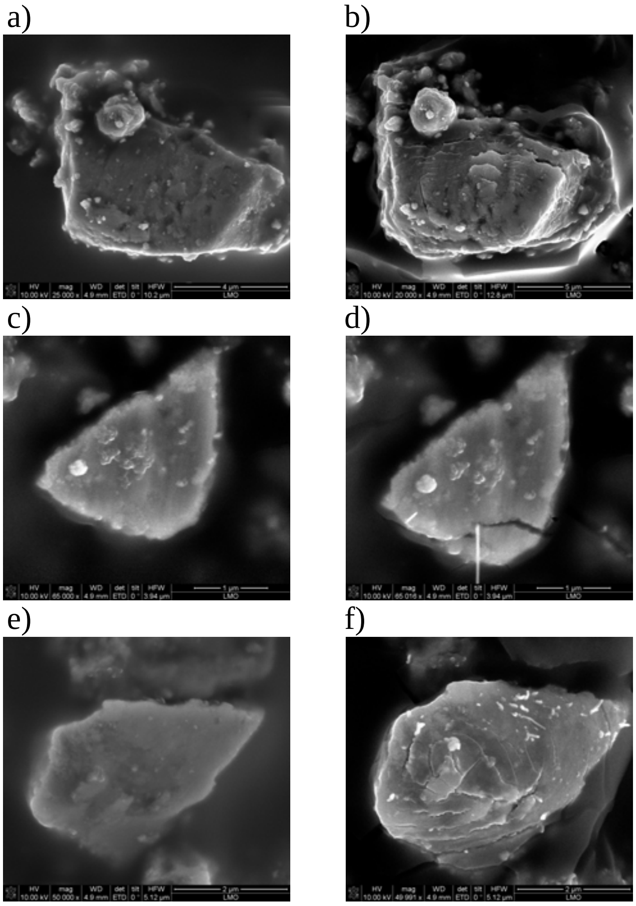

Fig. 15: *In situ* SEM investigations on three different mechanosynthesized Zn_2SnO_4 particles

a) initial state (left) and discharged to about 0.2 V in the first cycle (right)
b) discharged to 0,7 V (left) and discharged to 0.53 V (right), both in the first cycle
c) initial state (left) and discharged to 0.53 V in the first cycle (right)

It is visible in all pictures that in the course of discharging a significant cracking of the particles occurs. The first cracking was observed at 0.53 V. The cracks occur at a state of charge at which there is no alloying product visible in the XRD pattern (The situation at 0.53 V can be correlated to the state with x=8.5 measured with XRD). At 0.53 V furthermore one can detect whiskers which grew out of the particles (example in Fig. 11b). In consideration of the XRD results these are very likely metallic Zn and/or Sn whiskers. So there is a creation of metallic products in the first reduction reactions as well as side reactions which form for instance Li_2O. Both probably lead to strain in the particles which results in cracking. The metallic parts then partially burst out of the particle and grow in the shape of whiskers. The result of this growing process can also be seen in Fig. 16 which shows a particle at the very end of the cycling process. Several whiskers are grown with remarkable length compared to the particle size. By growing out the – most likely – metallic parts become separated and thus they react independently in the following cycling. Due to the known low cycling performance of metallic Zn and Sn this contributes to the general decrease in capacity.

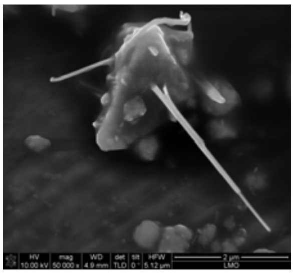

Fig. 16: Mechanosynthesized Zn_2SnO_4 particle at the very end of the cycling process

Mössbauer spectroscopy was performed on mechanochemically prepared Zn_2SnO_4 before and after insertion of Li, cf. Fig. 17. The initial spectrum shows a peak at 0 mm/s characteristic of Sn^{4+} in the SnO_6 tetrahedra of SnO_2. After Li insertion this peaks disappeared completely and a new broad peak appeared at 2.1 mm/s. This value is characteristic of Sn^0, i.e. metallic Sn in Sn metal or Sn alloy environments.

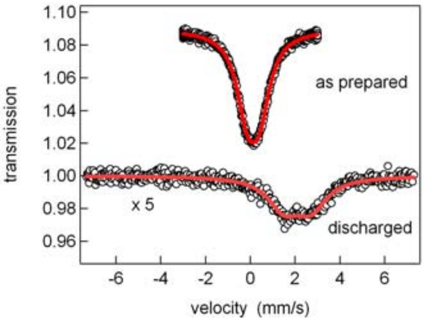

Fig. 17: Sn Mössbauer spectra of mechanosynthesized Zn_2SnO_4 before and after insertion of Li.

3. SnO_2/C Nanocomposites

Nanocomposites based on SnO_2 with carbon scaffold were used as highly porous anode films on Ni substrates. The films were obtained by *in situ* deposition of the particles without any binder or excess carbon black avoiding any secondary treatment. Compared to similarly prepared uncoated SnO_2 nanoparticles as well as conventionally prepared powder samples the capacity loss of the *in situ* deposited nanocomposite films is significantly reduced. Thus, this newly developed anode material combined with *in situ* film formation is a promising approach for high capacity anodes in Li-ion batteries.

SnO_2 nanoparticles as well as nanocomposites based on this oxide and carbon have been synthesized utilizing the Karlsruhe Microwave Plasma Process (KMPP), a gas-phase synthesis method described elsewhere. For the utilization as negative electrode material in Li-ion batteries the nanocomposite particles have been deposited *in situ* as a nanoparticle film on Ni-Substrates according to the method described in previous work. As precursor for the core particles tin-tetrachloride ($SnCl_4$), and for the carbon shell 1,3-Dicyclopentadiene ($C_{10}H_{12}$) were employed. The relevant synthesis parameters used in the context of this work were precursor feeding rates 5 ml/h of $SnCl_4$, 5 ml/h of dicyclopentadiene for a thick coating, 1 ml/h of dicyclopentadiene for a thin coating, gas flow (20% O_2 in Ar) of 5 l/min, microwave power of 600 W for the core particles (first reaction stage) and 340 W for the shell (second reaction stage), preheat time of 5 min and coating time of the substrates of 15 min. In a typical run 4 ml of $SnCl_4$ and appropriate amounts of dicyclopentadiene were used.

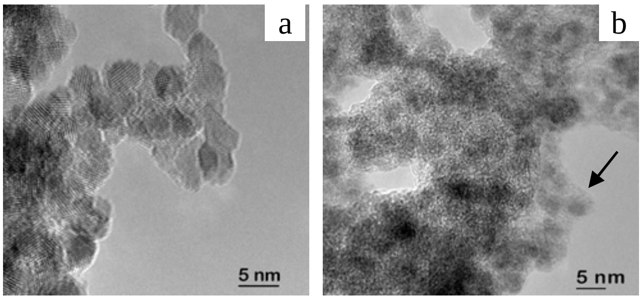

Fig. 18: TEM: Bright field image of SnO_2/C nanoparticles. (a): thin coating, lattice fringes of SnO_2 are visible, carbon shell is difficult to detect. (b): thick coating, carbon shell is clearly visible (arrows).

TEM of the so produced particles (Fig. 18) shows a relatively uniform particle or core size of about 5 nm. The shape of the particles is typically spherical. The characterisation of the carbon shell of the SnO_2/C nanocomposites is much more elaborate. In case of the thin coating (Fig. 18a) the shell is difficult to detect. This difficulty results mainly from the fact that the carbon coating is assumed to be thinner than the resolution of the microscope (0.24 nm). Additionally, it is amorphous and provides only weak interaction with the e^- beam due to the low atomic number. In case of the thick coating (Fig. 18b) the shell is clearly visible but it is not possible to determine a well-defined thickness of this shell. Anyhow, even the thin carbon coating can be detected clearly using electron energy loss spectroscopy (EELS) which is shown in Fig. 19. Comparing the low loss spectrum with reference spectra of amorphous carbon and bulk SnO_2, carbon identification is not easily done. However, the carbon signal is clearly visible in the core losses. As the spectra were acquired on sample areas lying over holes of the grid covering holey carbon film, the carbon signal definitely stems from the sample, and not from the carbon film. Complementary gravimetric determination of carbon content yields 16.7 wt.% for the thin, and 63.5 wt.% for the thick coating, respectively.

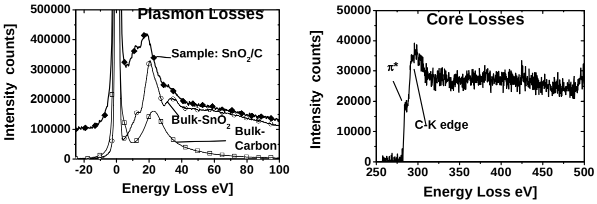

Fig. 19: Electron energy loss spectra of SnO_2/C core/shell nanoparticles with thin carbon shell. For better visibility, the plasmon loss spectra are stacked. The bulk-spectra herein show reference spectra to clarify the peak positions. The presence of the carbon coating can be proved in the core losses.

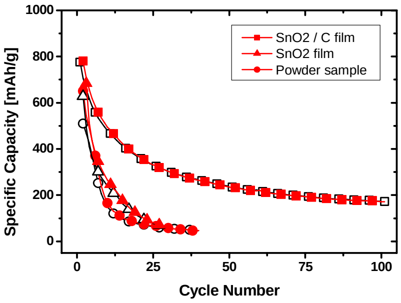

Fig. 20: Charge (black open symbols) and discharge (red filled symbols) capacity of different SnO_2 nanoparticle electrodes vs. cycle number. Comparison of an *in situ* deposited film of C-coated SnO_2 particles with thick C-shell, an *in situ* deposited film of uncoated SnO_2 particles, as well as a conventionally powder processed sample.

In Fig. 20 the specific capacity of different SnO_2 nanoparticle electrodes is shown vs. cycle number. The first discharge step, where the irreversible reaction $SnO_2 + 4\ Li \rightarrow Sn + 2\ Li_2O$ takes place, is not shown. The first reversible specific capacity was determined for all samples in the region of about 780 mAh/g, showing a good agreement with the theoretical value. This means at least for the first reversible cycle that all the deposited material is accessible for the Li-ions, i.e. contributes to the storage capacity. With increasing cycle number the capacity drops for all samples. This capacity loss is attributed to internal stress caused by the large volume change during the alloying process from Li and Sn to $Li_{22}Sn_5$ resulting in cracks and loss of active material. The most drastic capacity drop is observed for the conventionally powder processed sample. The capacity of the electrodes made with *in situ* deposited uncoated particles decreases also, but not as fast as for the powder sample. The capacity fading of the electrodes made with *in situ* deposited C-coated particles is least pronounced. Thus, it was possible to retain 50% capacity after 25 cycles and 25% after 100 cycles. Though not yet sufficiently stable for technical applications, the observed cycle stability is in the range of typical tin-based materials but without the need of any binder and secondary treatment.

4. In situ SEM studies

A novel experimental concept was developed for the *in situ* SEM investigating of electrodes for lithium-ion batteries. It uses an ionic liquid based electrolyte which allows the operation of a special battery under vacuum. With this it is possible to observe a battery inside an SEM under high resolution. This concept could be possibly adapted to other investigation methods such as transmission electron microscopy or photoelectron spectroscopy. Using this method, experiments on SnO_2 were performed that reveal some of the active mechanisms in this material and show that the electrochemical behavior of this material strongly depends on particle size.

A region of the electrode containing small particles with dimensions below 100 nm is shown in Fig. 21. It may be assumed that the changes in volume are more or less isotropic so that the three-dimensional volume changes can be estimated from the two-dimensional area changes. Upon insertion of lithium into the SnO_2 particles, the volume of the particles increased more than one order of magnitude. The increase in particle size occurred within the first few cycles with the change that happened within the first cycle being the largest one. At times when lithium was extracted, no growth or shrinkage could be seen. Depending on imaging conditions, brighter and darker regions could be identified on the particles. During the first few cycles, the darker shell increased in thickness and then stabilized. The brighter part in the center of the particles slightly decreased in size over the course of several cycles.

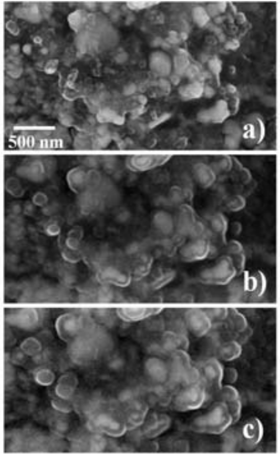

Fig. 21**:** SnO_2 particles at initial state (a), after first insertion of lithium (b) and after the second insertion (c). The images have the same magnification.

On the larger particles, different observations were made. These particles also showed a strong increase in size as can be seen from Fig. 22. This increase was accompanied by a blurring of the edges and a rounding of the corners. Shells as observed on the smaller particles did not seem to form. Although the volume increase was significant, it was smaller than that of the small particles as can be seen by comparing Fig. 21 with Fig. 22. This volume increase also was observed to be irreversible. In the larger particles, cracks were found quite frequently (Fig. 22) whereas no cracks were seen in the smaller particles.

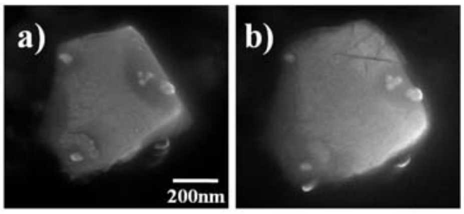

Fig. 22: Single SnO_2 particle before (a) and after the first lithium insertion (b). Besides the volume expansion, cracks and extrusions (lower left) appeared on the particle surface after the first lithium insertion.

5. Sputtered SnO_2 Thin films

We prepared thin films of SnO_2 with grain sizes in the nanometer range by radio-frequency (RF) sputtering to study the influence of morphology on the battery performance. The porosity of the films could be varied via the oxygen content in the plasma and via the power of the applied RF field. The films were deposited on to stainless steel as well as Si(100) substrates with a 3-inch SnO_2 target of 99.9% in purity. The substrates were sputter cleaned at -300 V self bias in a pure Ar plasma before film growth. During deposition, the substrate holder was electrically grounded and not externally heated, positioned 13 cm below the target. Ar/O_2 gas mixtures of different compositions, with 100 sccm total flow rate and correspondingly at 0.55 Pa pressure, were used for the deposition. The resulting film thickness was determined by a surface profilometer KLA Tencor P-10 to be about 1.5 μm. Figure 23a shows the voltage profile of the SnO_2 film prepared at an oxygen content of 10 % and a radio-frequency power of 150 W. During the first discharge an irreversible capacity loss of 500 mAh/g appears. This can be assigned to the formation of a passivation layer, the so-called solid-electrolyte interface, at the electrode surface which irreversibly consumes Li. During the following cycles the shape of the voltage profile is more stable and the coulombic efficiency is close to 100 %, i.e. the Li that is removed from the working electrode during charging is completely re-inserted in the subsequent discharging process. The losses in the capacity that are observed during extensive cycling occur during the charging processes, i.e. the active electrode material is not fully re-oxidized.

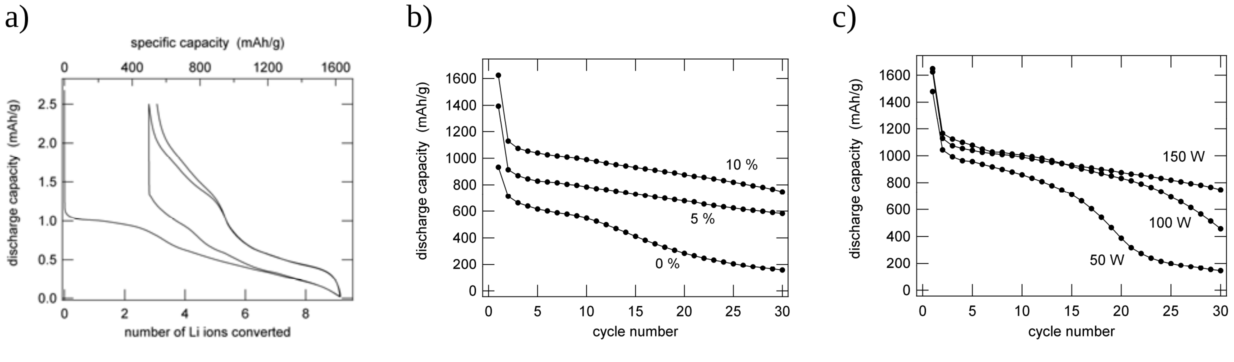

Fig. 23: a) The voltage profile during galvanostatic cycling for a sputtered SnO_2 film. b) The discharge capacity of SnO_2 thin films as a function of cycle number for an RF power of 150 W and different oxygen contents in the RF plasma. c) The discharge capacity of SnO_2 thin films as a function of cycle number for an oxygen content of 10 % and different RF powers.

The discharge capacity of the SnO_2 films for the first 30 cycles is plotted in Fig. 23b for different oxygen contents at a constant RF power of 150 W. Figure 23c shows the discharge capacity for different RF powers at a constant oxygen content of 10 %. The figures show that the discharge capacity in the first cycle is distinctly higher than in the subsequent cycles. This again reflects the formation of the solid-electrolyte interface. Furthermore, the figures show that the performance of the electrode materials can be improved drastically by increasing oxygen content during sputtering as well as by increasing the RF power. Additonal investigations on the morphology of the films by AFM and SEM show that the good electrode performance is correlated to a high roughness/porosity of the films.

References

[1] X. L. Fu, X. X. Wang, J. L. Long, Z. X. Ding, T. J. Yan, G. Y. Zhang, Z. Z. Zhang, H. X. Lin, X. Z. Fu, *J. Solid State Chem.* **182**, 517 (2009).

[2] J. Fang, A. H. Huang, P. X. Zhu, N. S. Xu, J. Q. Xie, J. S. Chi, S. H. Feng, R. R. Xu, M. M. Wu, *Mater. Res. Bull.* **36**, 1391 (2001).

[3] R. A. Huggins, *J. Power Sources* **81-82**, 13 (1999).

Own References

[F3.3:1] Local Structural Disorder and Relaxation in SnO_2 Nanostructures Studied by ^{119}Sn MAS NMR and ^{119}Sn Moessbauer Spectroscopy
S. Indris, M. Scheuermann, S. Becker, V. Šepelák, J. Suffner, C. Feldmann, A. Ulrich, H. Hahn, submitted.

[F3.3:2] A One-Step Mechanochemical Route to Core–Shell Ca_2SnO_4 Nanoparticles Followed by ^{119}Sn MAS NMR and ^{119}Sn Mössbauer Spectroscopy
V. Šepelák, K. D. Becker, I. Bergmann, S. Suzuki, S. Indris, A. Feldhoff, P. Heitjans, C. P. Grey, *Chem. Mater.* **21**, 2518 (2009).

[F3.3:3] Development of Nanocomposites for Anode Materials in Li-Ion Batteries
R. Ochs, D. V. Szabó, S. Schlabach, S. Becker, S. Indris, *Phys. Status Solidi* A, in press.

[F3.3:4] *In situ* SEM Studies on Lithium Ion Battery Electrodes Using Ionic Liquids
D. Chen, S. Indris, M. Schulz, B. Gamer, R. Mönig, submitted.

[F3.3:5] Influence of Oxygen Partial Pressure on the Formation of Tin (IV) Oxide Films
M. O. Guler, J. Ye, C. Ziebert, S. Ulrich, S. Indris, S. Lenhert, H. Hahn, H. Akbulut, submitted.